Journal of Materials Research and Technology 37 (2025) 2449–2462

Contents lists available at ScienceDirect

Journal of Materials Research and Technology

journal homepage: www.elsevier.com/locate/jmrt

Fast heating annealing of V-microalloyed TWIP steel: Pathway to ultrafine grains and enhanced mechanical performance

Atef Hamada [a,*], Ali Khosravifard [b], Tuomas Alatarvas [c], Matias Jaskari [a], Walaa Abd-Elaziem [d,e], Tarek Allam [f,1], Antti Järvenpää [a]

[a] Kerttu Saalasti Institute, Future Manufacturing Technologies (FMT), University of Oulu, Pajatie 5, FI-85500, Nivala, Finland
[b] Department of Materials and Metallurgical Engineering, Abadeh Higher Education Center, Shiraz University, Abadeh, 73916, Iran
[c] Process Metallurgy Research Unit, Centre for Advanced Steel Research, University of Oulu, P.O. Box 4300, FI-90014, Oulu, Finland
[d] Department of Mechanical Design and Production Engineering, Faculty of Engineering, Zagazig University, P.O. Box 44519, Egypt
[e] Department of Materials Science and Engineering, Northwestern University, Evanston, IL, 60208, United States
[f] Institute of Energy Materials and Devices - Structure and Function of Materials (IMD− 1), Forschungszentrum Jülich GmbH, 52428 Jülich, Germany

ARTICLE INFO

Keywords:
High-Mn TWIP steel
Fast annealing
Microstructure
Recrystallization
Mechanical properties
Physically based modeling

ABSTRACT

This study explores the effect of fast heating annealing (FHA) on the microstructure and mechanical properties of V-microalloyed high-Mn TWIP steel. Cold-rolled sheets were subjected to FA cycles at a heating rate of 200 °C/s over a temperature range of 700–900 °C for 30 s. The microstructures achieved through FHA were characterized using electron backscatter diffraction (EBSD), while mechanical performance was evaluated through uniaxial tensile testing and physically based modeling.

FHA at lower temperatures (700–800 °C) promoted partially recrystallized structures, while fully recrystallized ultrafine-grained microstructures were obtained at 850–900 °C. The optimized structure achieved at 850 °C showcased an exceptional strength–ductility balance, with a yield strength of 415 MPa, tensile strength of 850 MPa, and elongation of 60 %, resulting in a high UTS × TE product of 50700 MPa·%. Fractographic analysis revealed ductile failure dominated by dimple formation, with voids nucleated at non-metallic inclusions.

Inclusion classification and statistical analysis further identified Al_2O_3–Mn(S,Se) as the most dominant inclusion type, with complex multiphase clusters also observed, indicating their role in damage initiation. The applied mechanistic modeling and strain-hardening analysis confirmed that dynamic Hall–Petch strengthening, driven by mechanical twinning and grain refinement, significantly enhanced strain hardening and delayed plastic deformation instability.

These findings demonstrate that FHA offers a viable, time-efficient processing strategy for tailoring microstructure and optimizing the mechanical performance of high-Mn TWIP steels through controlled recrystallization, twin activation, and precipitation strengthening.

1. Introduction

Austenitic High-Manganese Twinning-Induced Plasticity (high-Mn TWIP) steels exhibit exceptional combinations of ultimate tensile strength (UTS) and ductility. This unique class of steel has garnered substantial attention for its potential in diverse applications, ranging from automotive components to structural elements [1–4]. The intricate interplay between microstructural features, precisely the grain size and the mechanical properties in these steels, serves as a pivotal area of exploration [5,6]. The performance and deformation mechanisms under tensile loading have been studied in numerous works, e.g., Refs. [7–11].

This investigation employed the fast heating annealing (FHA) processing after heavy cold rolling of the studied TWIP steel. FHA is a novel technology that involves high heating rates exceeding 100 °C/s and short annealing times to achieve a variety of grain sizes ranging from nano to ultrafine sizes. This technology allows for the precise control of the recrystallization fraction in cold-deformed steel, facilitating the use of recovery and partial annealing [12–15].

A uniform temperature exists throughout the material during equilibrium heating of the steel. As a result, the equilibrium transformation

* Corresponding author at: Kerttu Saalasti Institute, Future Manufacturing Technologies (FMT), University of Oulu, Finland. Tel.: +358 45 251 6553.
E-mail addresses: atef.hamadasaleh@oulu.fi, atef.hamada@gmail.com (A. Hamada).
[1] On an unpaid leave from Department of Metallurgical and Materials Engineering, Suez University, 43528, Suez, Egypt.

https://doi.org/10.1016/j.jmrt.2025.06.164
Received 15 January 2025; Received in revised form 26 May 2025; Accepted 21 June 2025
Available online 23 June 2025
2238-7854/© 2025 The Authors. Published by Elsevier B.V. This is an open access article under the CC BY license (http://creativecommons.org/licenses/by/4.0/).

of ferrite and cementite into austenite occurs when heating the entire material. Moreover, the austenite phase displays a consistent distribution of carbon and other alloying elements. However, the FHA of the steel at the aforementioned rates leads to a non-uniform distribution of chemical elements and even phases composition. The heating rate also affects the recrystallization of the new austenite phase. Recrystallization occurs completely in the initial ferritic regions when the cold-worked steel is heated slowly (conventional processing). Thus, austenite grains predominantly form at the prior grain boundaries during heating. However, at high heating rates, a greater number of austenite nuclei can form even in the recovered or partially recrystallized regions [16]. These refined austenitic grains may lead to a refined final microstructure upon cooling after the annealing process [17].

In the existing literature, FHA processing has predominantly found applications for carbon steels, dual-phase steels, and quenching & partitioning steels, contributing to refined grain structures and subsequent improvements in mechanical properties [12,18–21]. Matlock et al. [22] have also reviewed the influence of so-called fast thermal processing, i.e., processes involving FH or cooling, on advanced high-strength steels (AHSSs). Notably, there are scarce FHA studies specifically focused on high-Mn TWIP steels. In our previous investigation, we implemented FHA on a cold-rolled Fe-0.01C-21.3Mn–3Al–3Si steel heated to a temperature range of 650–1200 °C for short durations (2–180 s) [23]. A significant grain refinement at low temperatures of FHA was achieved. In a similar context, the double-reversion annealing, a two-stage cold rolling process, and subsequent FA by fast induction heating to create a bulk nano-grained structure in austenitic stainless steel (Type 301LN) were employed [24,25]. Recently, ultra-flash heating cycles have been applied to S900 steel, achieving an exceptionally FH rate of 1000 °C/s to reach temperatures of 550 and 650 °C, which have led to the predominant promotion of nano-scale precipitates along the block and packet boundaries of the martensite [26].

In AHSSs, FHA promotes the segregation of alloying elements, most notably Mn, within the intercritical austenite. This phenomenon is primarily attributed to the inherently slow diffusion kinetics of Mn in these steels [27]. Chemical heterogeneity is generally undesirable in the metallurgy of steels. However, the partitioning of alloying elements, especially that of Mn, has been recently used in controlling the microstructure of AHSSs to achieve improved mechanical properties [28,29]. It has been shown that the heterogeneity of Mn in the intercritical austenite strongly affects the stability of this phase and the subsequent formation of ferrite during cooling [27].

As highlighted in the literature above, despite the well-documented advantages of FHA in conventional carbon and dual-phase steels, its application to high-Mn TWIP steels remains largely unexplored. FHA is a fast thermal processing technique that utilizes exceptionally high heating rates (typically HR > 100 °C/s) and short dwell times to enable fine control over recrystallization behavior and grain size evolution. This approach sharply contrasts with conventional annealing, as shown in Fig. 1, which often requires longer durations and slower heating rates of less than 10 °C/s, resulting in coarser microstructures and limited flexibility in tuning mechanical properties. In high-Mn TWIP steels, where mechanical twinning governs deformation behavior, the ability to tailor grain structure via FHA offers a promising pathway to overcome the traditional strength–ductility trade-off. This study pioneers the use of FHA in V-microalloyed high-Mn TWIP steels. It demonstrates that optimizing the annealing temperature and leveraging fast thermal cycles can produce ultrafine and partially recrystallized structures that deliver enhanced yield strength (YS), ductility, and strain-hardening response. This work provides critical insights into the potential of FHA as a transformative processing route for next-generation high-strength austenitic steels.

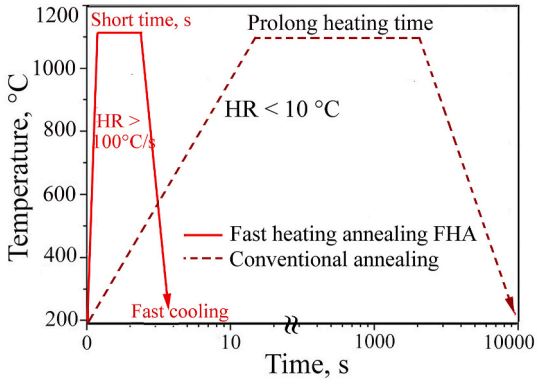

Fig. 1. The schematic illustration depicts the time-temperature cycles for FHA, which features FH and a short duration compared to conventional annealing. HR: heating rate.

The FHA technique has emerged as a novel thermal processing method in steel metallurgy, offering significant advantages over conventional annealing, particularly in terms of time efficiency, energy savings, and control of microstructural characteristics. FHA typically employs heating rates exceeding 100 °C/s and extremely short dwell times, facilitating fast microstructural transformation under nonequilibrium conditions. In contrast, conventional annealing methods involve slow heating rates and prolonged holding times, as schematically illustrated in Fig. 1, often resulting in coarse grains and limited flexibility in tuning mechanical properties. While FHA has been explored for carbon, dual-phase, and quenching-and-partitioning steels, its application in high-Mn TWIP steels is still limited, especially with microalloying elements like V. This study addresses that gap by applying FHA to a V-microalloyed high-Mn TWIP steel and systematically investigating its effects on recrystallization behavior, grain refinement, and mechanical performance. This work aims to clarify how FHA can serve as a transformative, industrially viable alternative to conventional processing routes in TWIP steels, particularly for enhancing the strength–ductility synergy without prolonged thermal cycles.

2. Experimental procedures

2.1. Material

The high-Mn TWIP steel used in this study was produced at the pilot plant of ThyssenKrupp Steel Europe AG (TKSE), located in Germany. The steel was manufactured through a controlled melting process conducted in an induction furnace operated under an argon atmosphere. The melting temperature was set at 1600 °C. The raw materials employed in the steel production consisted of the following components: iron, electrolytic Mn, commercially pure Al, ferro-vanadium, and ferrocarbon. These materials were carefully selected to achieve the desired composition for the high-Mn TWIP steel. Subsequently, the molten steel was cast into 15 kg ingots using a steel mold with 3600 mm × 200 mm × 30 mm dimensions. The chemical composition of the investigated steel is presented in Table 1.

2.2. Material processing and mechanical properties

To investigate the mechanical properties, the steel ingots underwent a homogenization treatment at 1200 °C for 1 h. The ingots were then hot-rolled using a pilot rolling mill to produce sheets with a final thickness of 4 mm. These sheets were further cold rolled with a 70 % reduction, ultimately reaching a final thickness of 1.2 mm. This cold rolling process induced a true strain of approximately 1.2.

Table 1
Chemical composition of the investigated high-Mn TWIP steel.

element	Mn	Al	C	V	N	Fe
wt.%	20.0	1.5	0.61	0.3	0.003	Bal.

The cold-rolled sheets were subjected to FHA treatments at temperatures ranging from 700 °C to 900 °C for 30 s. The FHA treatments were conducted using a Gleeble 3800 thermomechanical simulator, which enables precise thermal control through a closed-loop feedback system. A K-type thermocouple was spot-welded at the center of the gauge section on one side of each tensile specimen to provide accurate, real-time temperature monitoring. The thermal profiles were pre-calibrated using dummy samples of identical dimensions to ensure temperature uniformity and reduce overshooting. The heating rate was maintained at 200 °C/s through resistance heating, and the system's feedback mechanism actively adjusted the current input to keep the target annealing temperature within ±5 °C. This setup ensured consistent heating and minimized thermal gradients across the gauge length during the short 30 s dwell time.

Fig. 2 provides a schematic illustration of the applied thermomechanical cycle experienced by the steel. Through controlled static recrystallization (SRX), the resulting grain structures are identified by codes corresponding to their respective temperatures: T700, T750, T800, T850, and T900. The quasi-static mechanical properties at room temperature were determined through uniaxial tensile tests conducted at a strain rate of 10^{-3} s^{-1}, utilizing a Zwick Z 100 tensile machine (Zwick Roell, GmbH). Tensile testing specimens were prepared following ASTM E 646–98, featuring a parallel length of 15 mm, a gauge length of 10 mm, a width of 6 mm, and a total length of 180 mm.

2.3. Microstructure characterization

The detailed microstructures of the FHA were analyzed via electron backscatter diffraction (EBSD) utilizing a field-emission scanning electron microscope (FE-SEM, Zeiss Ultra Plus). EBSD mapping was performed at an accelerating voltage of 15 kV with a step size of 0.01 μm. To obtain comprehensive statistical information on the distribution of grain sizes, the EBSD data were processed using HKL CHANNEL 5 software (Oxford Instruments). Grain reconstruction was performed with a minimum grain size of 5 pixels and a critical misorientation threshold of 15° to define grain boundaries. Grain size was determined using the equivalent circle diameter (ECD) based on individual grain areas. To evaluate recrystallization behavior, the grain orientation spread (GOS) method was used: grains with GOS <2° were considered recrystallized, 2°–5° as substructured, and >5° as deformed. These criteria allowed quantitative analysis of recrystallization fractions across different FHA temperatures. This approach allowed for a detailed examination of the microstructural characteristics of the annealed specimens.

EBSD data were collected from at least three distinct regions across the central gauge length of each annealed specimen to ensure statistical representativeness. Each scan covered an area of approximately 50 × 50 μm^2, and care was taken to avoid areas near the specimen edges or those with visible surface artifacts. The selected regions consistently displayed similar microstructural features, confirming that the analyzed areas represented the overall microstructure induced by each annealing condition. This approach enabled reliable quantification of grain size distributions and recrystallization fractions.

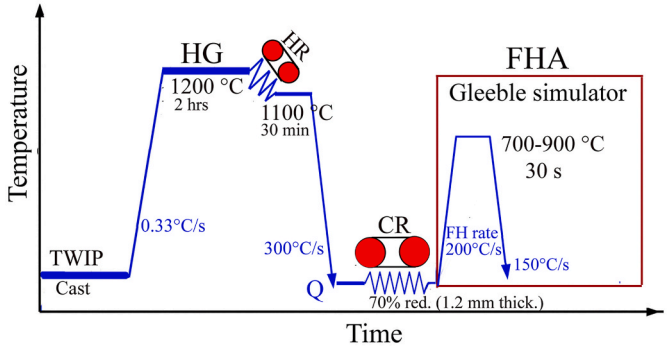

Fig. 2. Schematic illustration of the thermomechanical cycles applied to the steel, involving FA treatments at 700–900 °C for 30 s. The cycle includes the following stages: HG: homogenization, HR: hot rolling, FH: fast heating, Q: water quenching, and FHA: fast heating annealing.

2.4. Non-metallic inclusions extraction and characterization

The presence and characterization of non-metallic inclusions (NMIs) in the TWIP steel were studied by applying a controlled electrolytic extraction method. A steel sample was cut into a rectangular piece measuring approximately 10 mm × 10 mm × 5 mm. Its surface was carefully ground using an MD Piano 600 disc to create a smooth, clean, and oxide-free surface, which is essential for effective electrochemical dissolution.

The extraction was performed in a specially prepared electrolyte of 10 vol% acetylacetone, 1 wt.% tetramethylammonium chloride, and methanol as the solvent. The process was carried out under potentiostatic control at 0.15 V versus a standard calomel electrode, utilizing a BioLogic SP-150 potentiostat. During the 3-h extraction period, a stable current of about 25 mA was maintained, leading to the dissolution of roughly 0.1 g of the steel matrix. This enabled the NMIs to be selectively retained in the electrolyte.

The electrolyte was filtered through a membrane with a pore size of 0.8 μm to isolate the inclusions. The collected inclusions were subsequently examined using a Zeiss Ultra Plus field-emission scanning electron microscope (FE-SEM) equipped with an energy-dispersive X-ray spectroscopy (EDS) system. This enabled detailed compositional and morphological characterization of the extracted NMIs.

2.5. Modelling the flow behavior of different grain structures of TWIP steel

A phenomenological model considering the formation of mechanical twins and their influence on the dislocation motion is evaluated here to model the stress-strain curves obtained for different grain sizes. In other words, mechanical twinning introduces a so-called dynamic Hall-Petch effect in the austenite grains by reducing the mean free path of the dislocations during deformation. This is considered via a physically based model developed by Bouaziz et al. [30]. The flow stress of the material comprises three terms as follows:

$$\sigma = Y + \sigma_f + \sigma_b \quad (1)$$

where Y is the initial YS and depends on the lattice friction stress, σ_f, and σ_b are the isotropic and kinematic hardening, respectively. Isotropic hardening is related to the square root of dislocation density and can be calculated by the following equation:

$$\sigma_f = \alpha \cdot M \cdot G \cdot b \cdot \sqrt{\rho} \quad (2)$$

α is a constant, M is the Taylor factor, which relates the macroscopic strain of the specimen to the dislocations shearing, G is the shear modulus, b is the magnitude of Burgers' vector, and ρ is the density of dislocations. On the other hand, kinematic hardening in TWIP steels is mainly caused by the reduction of dislocations' free path, which itself is due to the formation of mechanical twins during the deformation. Therefore, this part of the flow stress is modeled using Eq. (3):

$$\sigma_b = M \frac{G \cdot b}{L} \cdot n \quad (3)$$

where L is the mean free path of the dislocations and n is the average number of dislocation loops in grains. The two parameters ρ and n are calculated versus strain according to the following equations:

$$\frac{d\rho}{d\varepsilon} = M \cdot \left(\frac{1}{b \cdot L} + H \cdot \sqrt{\rho} - R \cdot \rho \right) \quad (4)$$

$$\frac{dn}{d\varepsilon}=\frac{W}{b}\left(1-\frac{n}{n_0}\right) \quad (5)$$

where H and R are the hardening (dislocation accumulation) and recovery (dislocation annihilation) constants, respectively, W is the mean spacing between slip bands and n_0 is the maximum number of dislocation loops. Values as high as 8.0 has been given to n_0 in similar work [31], but here a value of 4.0 is used for this parameter due to the fine-grained SRX structures.

A MATLAB code is developed to solve the differential eqs. (4) and (5) where the former is solved numerically considering an initial value of $10^{12}/m^2$ for the dislocation density. Finally, the mean free path of dislocations (L) is calculated by considering the simultaneous effect of grain and twin boundaries:

$$\frac{1}{L}=\frac{1}{d}+\frac{1}{\lambda} \quad (6)$$

In this equation, d is the average grain size which is here obtained from the microstructural analyses (EBSD) and λ is the mean twin spacing. The latter is calculated according to Fullman's stereological analysis [32]:

$$\frac{1}{\lambda}=\frac{1}{2t}\frac{F}{1-F} \quad (7)$$

where t and F are twin width and volume fraction, respectively. The latter is equated to an exponential function of the form: $F = F_0(1-\exp(-\beta(\varepsilon-\varepsilon_i)))^m$ in which F_0, β and m are constants and ε_i is the twinning initiation strain. The values of the latter are extracted from Ref. [30]. The model parameters obtained for samples which were annealed at different temperatures are presented in Table 2.

3. Results and discussion

3.1. Microstructural evolution

As previously detailed in the experimental section, the cast steel was subjected to hot and cold rolling to produce cold-rolled sheets with a 70 % reduction. Subsequently, these sheets underwent FA treatment at different temperatures. This section illustrates the microstructural changes induced by FA at 700–900 °C for 30 s.

In Fig. 3, the microstructural evolution of the high-Mn steel following FA at 700 °C for 30 s is depicted. The image quality (IQ) map in Fig. 3(a) reveals insufficient pattern indexing in deformed areas, primarily caused by the highly strained regions that are characteristic of high dislocation density. Prominent black lines and inadequately indexed regions, correlating with slip bands and highly strained zones, highlight a lack of SRX in these areas under these conditions. This observation aligns with findings in previous studies on high-Mn steels with varying alloying elements, where numerous slip bands and high dislocation densities were reported to impede the indexing of backscattered patterns in the grain structure [33]. Fig. 3(b) presents a corresponding map, categorizing the grain structure into deformed, substructured (recovered), and recrystallized fractions. It is observed that the majority of the grain structure is highlighted in red, indicating deformed grains. The black regions in Fig. 3(a) correspond to mixed areas of varying colors on the map. Notably, a few fine grains appear in blue, signifying recrystallized grains predominantly located along grain boundaries of the deformed grains. Additionally, a small fraction of grains in yellow indicates recovery softening, promoting substructure/subgrains with low-angle grain boundaries (LAGBs, misorientation <15°).

Fig. 3(c) shows a magnified view of a colony with fine recrystallized grains. An important observation is the presence of recrystallized grains inside certain grains. The extent of recrystallization varies among grains, with grains labeled A and B showing no signs of recrystallization. This indicates that local differences in stored energy or crystallographic orientation may affect the observed recrystallization levels in adjacent grains. However, additional analysis is necessary to clarify the specific impact of grain orientation on the kinetics of SRX.

Fig. 3(d) illustrates the proportions of the promoted substructure attributed to recovery and newly recrystallized grains from SRX in comparison to deformed grains. At 700 °C for 30 s, the grain structure predominantly comprises 60 % deformed grains, while the fraction of recrystallized grains is comparatively low at 18 %.

In this context, some researchers have applied conventional SRX annealing to high-Mn TWIP steels at the relatively low temperature of 700 °C to promote an ultrafine-grained structure. However, it is essential to note that our comparison of the current SRXed microstructure achieved by FH to the literature is qualitative in nature, as the SRXed microstructure can be significantly influenced by variations in the composition of TWIP steels and differences in the extent of rolling deformation. Therefore, we aim to highlight general trends and phenomena observed at 700 °C rather than drawing definitive conclusions. Brack et al. [34] observed the promotion of a fully recrystallized microstructure in cold-rolled Fe–22Mn-0.6C (wt.%) steel during annealing at 700 °C for 100 s, yielding an average grain size of 3.5 μm. However, Liu et al. [35] observed that the complete recrystallization of Fe–24Mn–0.7Si–1.0Al TWIP steel required an extended duration of 5 min at 700 °C. It is well established that the alloying chemistry, primarily related to stacking fault energy, along with the degree of cold reduction and grain size, significantly influences the SRX kinetics of high-Mn steels [36–38].

Furthermore, the present steel is a V-microalloyed with a 0.3 wt.% V. Scott et al. [39] observed that at temperatures below 900 °C, highly dense and evenly distributed VC precipitates formed during annealing after cold rolling in high-Mn TWIP steel. Consequently, the recrystallization kinetics are expected to be influenced by the precipitation of VC in this instance. Zhang et al. [40] found that incorporating V into Fe–27Mn–8Al–1.0C lightweight austenitic steel promotes the formation of VC particles after a brief annealing at 900 °C following 60 % cold rolling. These particles significantly refined the grain structure, reducing it from 9.9 μm to 4.9 μm. In the same context, Yue et al. [41] reported the precipitation of a higher density of V_4C_3 carbides within the austenite matrix of TWIP steel sheets annealed at 700 and 800 °C after cold rolling. This finding suggests that these intermediate temperatures favor VC formation and contribute to recrystallization retardation and grain boundary pinning. Allam et al. [42] reported the formation of nanoscale VC-type precipitates in V-microalloyed MnCr TWIP stainless steel during a short annealing cycle at 1000 °C applied to cold-rolled sheets. The small size of the VC precipitates, approximately 20 nm, along with their high density, indicates a significant level of coherency with the austenite matrix.

The potential role of VC precipitates in retarding recrystallization kinetics is hypothesized based on prior studies on V-microalloyed TWIP steels. In particular, the observed partial recrystallization at 700–800 °C aligns with literature reports that VC carbides can form during annealing and serve as effective Zener pinning particles, impeding grain boundary migration. Our results are consistent with this mechanism.

Table 2
Parameters of the physically based model at various annealing temperatures.

Annealing temperature (°C)	d (μm)	ε_i	β	m	F_0	Y (MPa)
700	2	0.03	2	1.8	0.06	770
750	2.8	0.03	3	0.8	0.06	510
800	3.8	0.03	3.5	1	0.07	470
850	3.6	0.03	5	1	0.07	380
900	4.5	0.04	5	0.9	0.07	350

Parameters constant for all samples

n_0	α	G (GPa)	b (nm)	w/b	R	H	t (nm)	M
4	0.4	65	0.25	126	80	1×10^7	30	3.06

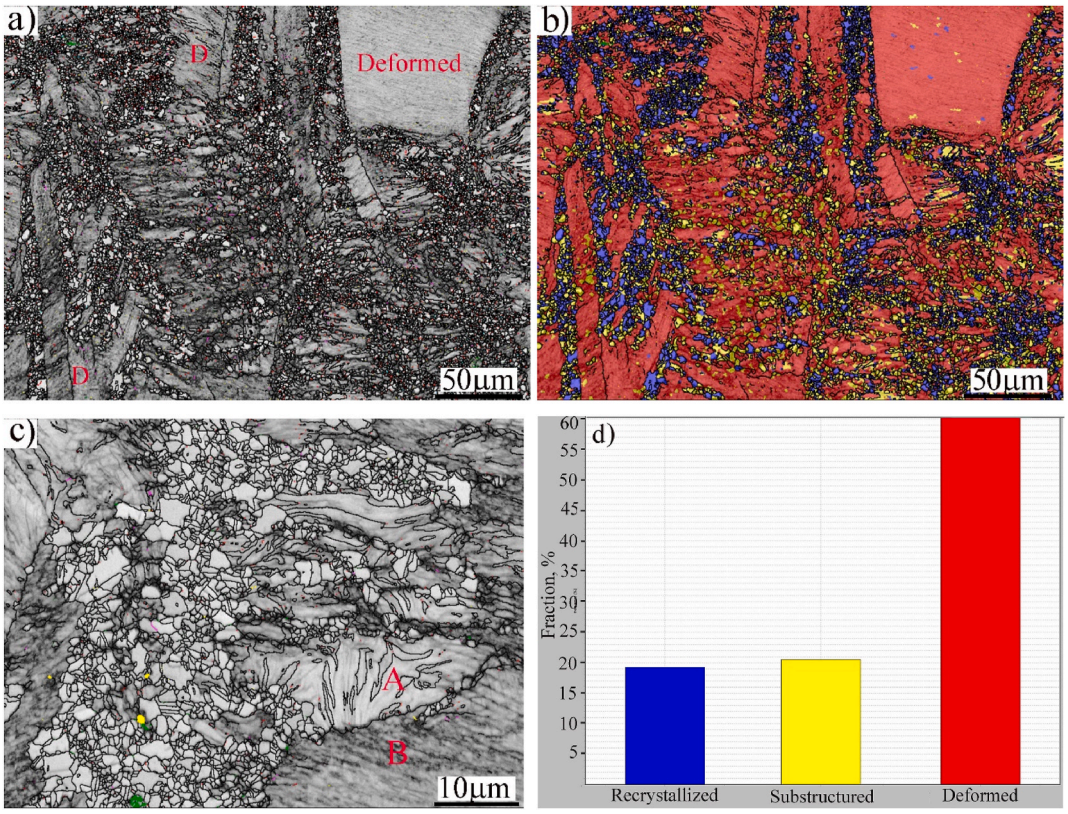

Fig. 3. EBSD mapping of microstructure evolution at 700 °C for 30 s: (a) IQ map, (b) REX map for the grain structure in (a), (c) high-magnification IQ map, and (d) recrystallized, substructured, and deformed grain fractions.

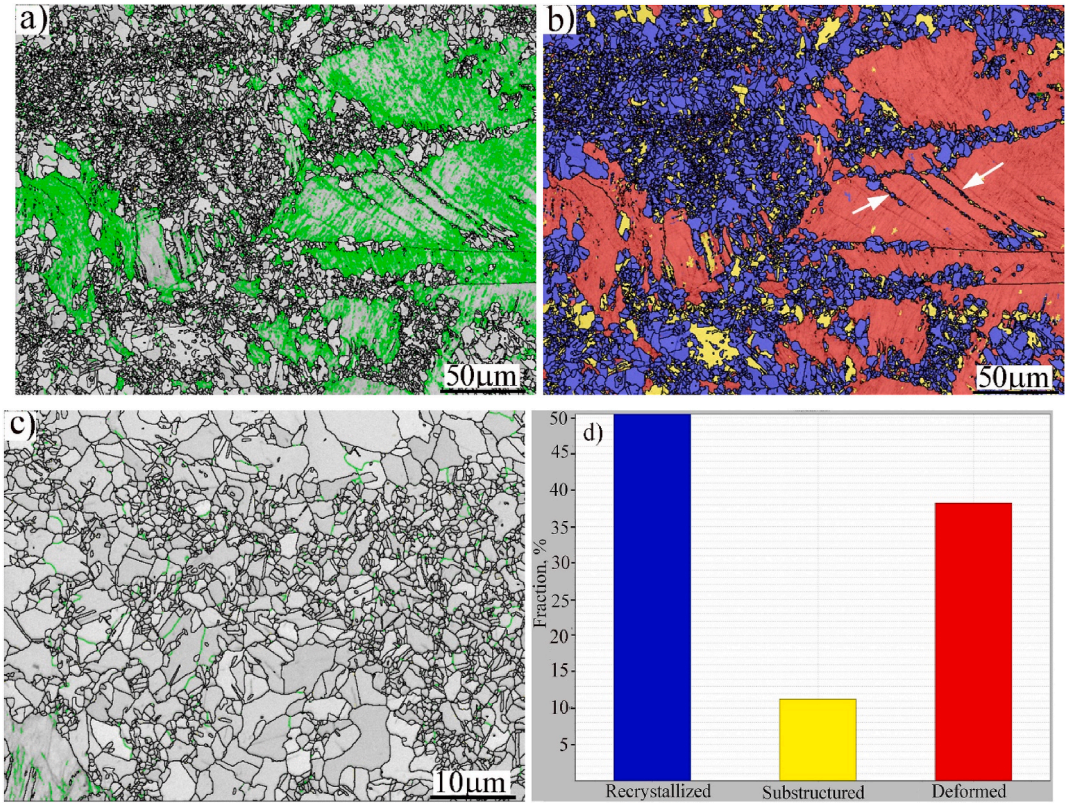

Fig. 4. EBSD mapping of microstructure evolution at 750 °C for 30 s: (a) IQ map superimposed with misorientation map, (b) REX map for the grain structure in (a), (c) high-magnification IQ map, and (d) recrystallized, substructured, and deformed grain fraction.

The FHA process preserves a high fraction (80 %) of deformed and substructured grains in the present study. These grains possess a high dislocation density, providing a large number of nucleation sites for VC precipitates. The precipitation effectively retards SRX. In a study related to the present work, Jo et al. [43] examined the impact of Al additions on the recrystallization kinetics of cold-rolled high-Mn steel containing V (Fe–15Mn–1Si-(0,0.5,1)Al-0.4C-0.3Mo-0.5V (wt.%)) and observed that the conventional annealing at 700 °C for 10 min still lead to partially recrystallized microstructures. The maximum volume fraction of recrystallized austenite reached 68.6 % in the steel with the highest Al content (1 %). The influence of Al was attributed to the increase of the stacking fault energy (SFE). However, the retarding influence of VC precipitation can be the reason for slow SRX kinetics. Upon increasing the FA temperature to 750 °C, the recrystallization rate is enhanced, as evidenced by Fig. 4. New ultrafine grains, alongside large grains shown in green, are present, as displayed in Fig. 4(a). Fig. 4(b) presents the corresponding REX map. The grains appearing in red signify deformed grains, where slip and deformation bands are evident. These slip bands serve as favorable sites for the nucleation of recrystallized grains, as indicated by the arrows. However, most of the SRX has occurred at the grain boundary regions (blue color). Fig. 4(c) provides a detailed view of the recrystallized grains, highlighting enhanced structural refinement by SRX. Moreover, the grain size within this region appears to be non-uniform, with an average size of 1.3 μm. This variation in grain size may be attributed to local differences in the degree of cold rolling, resulting in the heterogeneous nucleation of new grains during SRX. The corresponding REX map, depicted in Fig. 4(d), shows the microstructural changes after FHA at 750 °C. It reveals a substantial fraction of grains that have undergone SRX, accounting for approximately 50 % of the microstructure. This high percentage indicates the effectiveness of the annealing treatment at 750 °C in promoting the formation of new recrystallized grains within the material. Lan and Zhang [44] applied conventional slow heating and annealing treatments at various temperatures and durations to a high-Mn TWIP steel following a 60 % reduction in cold rolling. According to their findings, slow heating to 750 °C for 5 min promoted the formation of relatively large grains, averaging 10 μm in size. The significant disparity in grain size observed between the current study employing FHA and conventional annealing, as reported in the literature, highlights the benefits of employing FHA for enhancing microstructural grain refinement.

As the FA temperature is raised to 800 °C, SRX becomes more pronounced, leading to the promotion of a significant fraction of ultrafine grains, as depicted in Fig. 5(a). However, still, a few large deformed grains, labeled as A and B, persist. The corresponding REX map in Fig. 5 (b) illustrates these large grains in red, while the predominant blue regions signify recrystallized grains. Fig. 5(c) further demonstrates the substantial decrease in the fraction of deformed grains, from 60 % at 700 °C (Fig. 3(d)) to 16 % at 800 °C. Fig. 5(d) presents the grain size distribution of the SRXed structure achieved at 800°C. Approximately 28 % of the grains in the structure are less than 2 μm, and 60 % of the newly recrystallized grains are smaller than 5 μm. The estimated average grain size is 3 μm, reflecting the refined microstructure achieved in FHA processing. Nevertheless, a fully recrystallized microstructure was achieved at 800 °C for 100 s in a cold-rolled TWIP steel containing Nb microalloying (Fe–17Mn-0.6C-1.5Al-0.1Nb wt.%) [45]. This can be attributed to the longer annealing duration of 100 s. In the current study, the annealing duration was limited to 30 s to restrain the growth of newly recrystallized grains, which aligned with the primary objective of the FHA technology.

Upon increasing the annealing temperature to 900 °C, the microstructure exhibits a homogeneous distribution of fine equiaxed austenite grains without deformed grains, as shown in Fig. 6(a). According to the REX map in Fig. 6(b), most grains have experienced SRX, indicated in blue. Notably, no deformed grains are present; only a few small grains appear in yellow, suggesting subgrains, with a fraction of about 9 %, as depicted in Fig. 6(c).

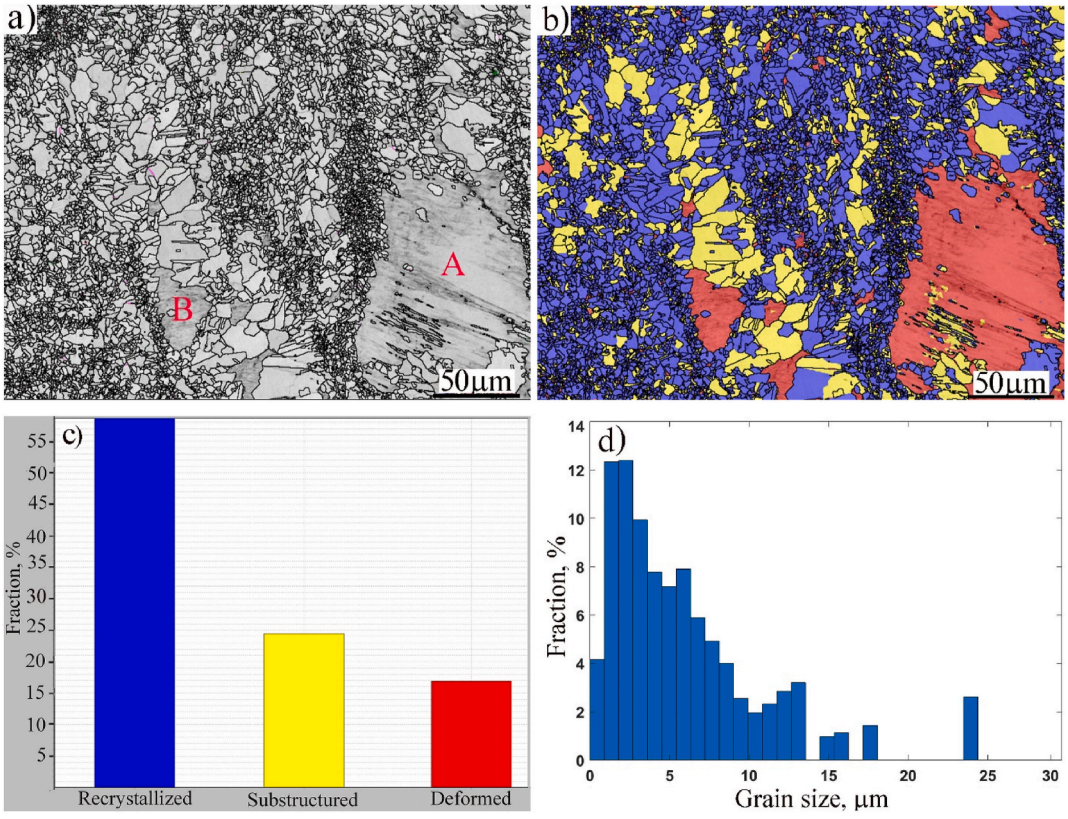

Fig. 5. EBSD mapping of microstructure evolution at 800 °C for 30 s: (a) IQ map, (b) REX map for the grain structure in (a), (c) recrystallized, substructured, and deformed grain fraction, and (d) grain size distribution of the grain structure in (a).

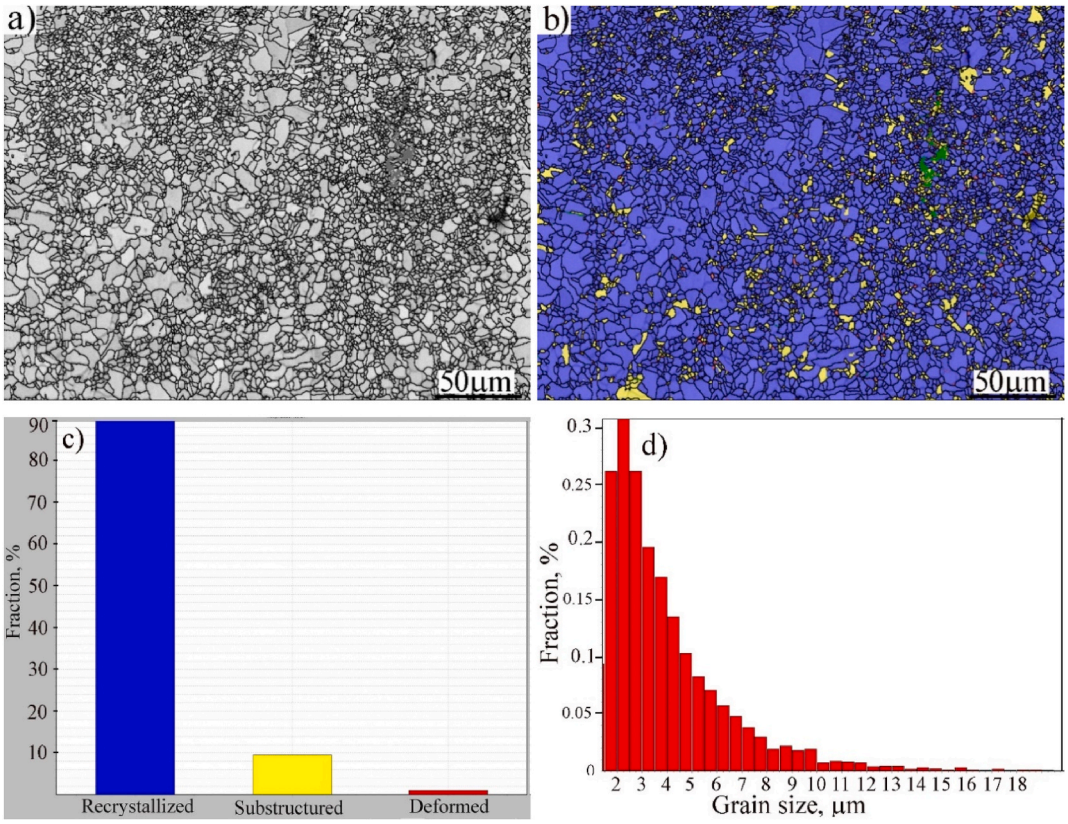

Fig. 6. EBSD mapping of microstructure evolution at 900 °C for 30 s: (a) IQ map, (b) REX map for the grain structure in (a), (c) recrystallized, substructured, and deformed grain fractions, and (d) grain size distribution of the structure in (a).

Fig. 6(d) examines the grain size distribution of the structure achieved after annealing at 900 °C. The new structure consists of 26 % grains that are less than 2 μm in size. A small fraction, approximately 10 %, displays sizes around 5 μm. Consequently, the average grain size of the SRXed structure at 900 °C is 4 μm, slightly larger than at 800 °C. Consistent with the findings of the present study, Kang et al. [46] observed complete recrystallization accompanied by grain growth up to 10 μm in cold-rolled Fe–18Mn–0.6C-1.5Al TWIP steel when conventionally annealed at temperatures above 850 °C, specifically at 900 °C. Similarly, Santos et al. [47] reported comparable recrystallization behavior and grain coarsening in Fe–24Mn–3Al–2Si–1Ni-0.06C steel.

The Hall–Petch relationship was applied to evaluate the contribution of grain boundary strengthening under various annealing conditions, offering a quantitative assessment of the effect of grain size on YS. The Hall–Petch equation is expressed as:

$$\sigma_y = \sigma_0 + k_y d^{-1/2} \tag{8}$$

where σ_y is YS, σ_0 is the lattice friction stress, k_y is the Hall–Petch slope, and d is the average grain diameter. Based on literature data for high-Mn TWIP steels, a Hall–Petch coefficient $k_y \approx 0.445$ MPa$\cdot m^{1/2}$ and $\sigma_0 \approx 158$ MPa were used [48]. For the T850 and T900 specimens, which exhibited fully recrystallized microstructures with average grain sizes of approximately 2.5 μm and 3.8 μm, respectively, the estimated YSs due to Hall–Petch strengthening were 439 MPa (T850) and 386 MPa (T900). These values are consistent with the experimentally measured YS, suggesting that grain refinement through FHA substantially enhances the YS. The difference in grain size between partially and fully recrystallized states also accounts for the gradual variation in strength across annealing conditions.

This quantitative analysis confirms that Hall–Petch strengthening is a dominant mechanism in FHA-treated TWIP steel and underscores the effectiveness of FHA in producing refined microstructures with enhanced strength.

3.2. Mechanical properties

To comprehensively understand the effect of FA, represented by a high heating rate of 200 °C and a short duration of 30 s, on the mechanical behavior of high-Mn steel, the tensile properties of the structures after FHA at temperatures ranging from 700 to 900 °C for 30 s were determined at room temperature.

In Fig. 7(a), the engineering stress-strain curves illustrate the flow stress behavior of various grain structures under tensile loading. An intriguing observation in the tensile stress-strain curves is the absence of serrations, which are typically observed in high-Mn TWIP steels due to dynamic strain aging during tensile testing [49–51]. A distinct enhancement in tensile properties is evident in the T700 structure, as depicted in Fig. 7(a). In V-microalloyed high-Mn TWIP steel, it is observed that a low annealing temperature (700 °C) promotes a partially recrystallized microstructure, which contributes to achieving a high YS, typically around 1 GPa [43]. Controlling the fraction of retained deformed grains, or hard regions, in the FHA-treated TWIP steel allows for achieving high YS and a satisfactory combination of tensile strength-elongation. Furthermore, the effect of V microalloying, primarily through the VC precipitation strengthening mechanism, complements the impact of partial recrystallization, resulting in an enhanced combination of mechanical strength and ductility in the steel. This is consistent with the literature that stated that the presence of unrecrystallized grains with high dislocation density and nano-scale mechanical twins in the low-temperature annealing of the cold-rolled high-Mn TWIP steel significantly contributes to strengthening [45]. When the FHA temperature rises to 750 °C, a noticeable decline in the flow stress curve occurs, accompanied by a marked improvement in ductility (see Fig. 7(a)). This phenomenon is attributed to a reduction in

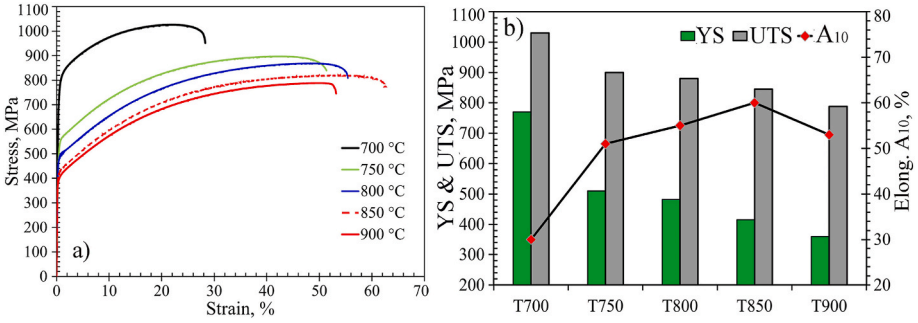

Fig. 7. Tensile mechanical properties at room temperature for various grain structures of the investigated TWIP steel, obtained at different annealing temperatures for 30 s duration: (a) Engineering stress-strain curves and (b) Extracted mechanical properties, encompassing yield strength (YS), ultimate tensile strength (UTS), and elongation across a gauge length of 10 mm (A_{10}).

the fraction of deformed grains, or hard regions, within the partially recrystallized microstructures, which decreases from 60 % at T700 to 38 % at T750 (see Figs. 3–4). Additionally, the degree of recovery at T750 is approximately double that at T700. Consequently, the level of softening in the microstructure at T750 is higher.

Similarly, increasing the FHA temperatures beyond 750 °C, reaching up to 900 °C, leads to a greater degree of softening, accompanied by a gradual decrease in the flow stress curves, as illustrated in Fig. 7(a). Fig. 7(b) displays the tensile properties values extracted from the stress-strain curves as a function of FA temperature.

Notably, the comparison reveals intriguing findings, especially in the case of the T700 structure annealed at 700 °C. This structure exhibits a noteworthy YS and UTS of 770 and 1030 MPa, respectively, accompanied by a moderate elongation of 30 %. In contrast, the T750 structure displays lower mechanical properties; however, the YS and UTS values remain relatively high at 510 and 900 MPa, respectively, with a substantial elongation of 50 %. For the structures promoted at T800 and T850, the YS values are still high, about 480 and 415 MPa, respectively, displaying a high elongation of 55–60 %. It seems that the FHA processing of high-Mn TWIP steel is beneficial in enhancing partial recrystallization, which enhances the strength and precipitation strengthening of VC. It is noteworthy that fully recrystallized coarse-grained high-Mn TWIP steels generally demonstrate a low YS of less than 300 MPa [10,52]. This corresponds to the fully recrystallized structure indicated in T900, with a low YS of 360 MPa and an elongation of 53 %.

The distinct processing conditions of FHA treatments, characterized by a FH rate of 200 °C/s and a short dwell time of 30 s, significantly impact the resulting microstructure and, consequently, the mechanical properties of the studied high-Mn TWIP steel. This technique markedly differs from conventional annealing methods by utilizing non-equilibrium thermal conditions to create refined and metastable microstructures.

At lower FA temperatures (700–800 °C), the thermal energy is sufficient to initiate static recovery and partial recrystallization, particularly along previous grain boundaries and areas of significant deformation. However, the limited thermal exposure prevents complete recrystallization, resulting in heterogeneous microstructures characterized by a high percentage of deformed grains. These deformed grains retain stored strain energy and elevated dislocation densities, which act as internal barriers to dislocation movement during deformation, significantly increasing YS. Simultaneously, the onset of recrystallization nucleation, along with reduced grain growth, promotes the development of ultrafine recrystallized grains (<2 μm) that enhance strength through grain boundary strengthening. The V-microalloying effect further enhances the microstructure. At these temperatures, fine VC precipitates form and serve as Zener pinning particles, hindering grain boundary migration and delaying complete recrystallization. Consequently, a thermally stable, partially recrystallized structure develops, exhibiting significant microstructural heterogeneity. This characteristic is advantageous for strain partitioning and mechanical twinning, both of which are essential to the TWIP) mechanism.

As the FHA temperature reaches 850–900 °C, the thermal driving force intensifies, encouraging bulk recrystallization and resulting in a fully recrystallized structure. However, the very short annealing time limits grain growth, preserving a fine equiaxed grain structure of approximately 2–4 μm. These smaller grains promote mechanical twinning during deformation, initiating the dynamic Hall–Petch effect, which causes twin boundaries to reduce the mean free path of dislocations, thereby enhancing work hardening. Consequently, the steel achieves a balanced combination of moderate YS and high tensile ductility. Crucially, FHA enables microstructural engineering without lengthy processing times or multiple annealing steps, highlighting a distinct advantage over traditional methods. The observed mechanical properties, which range from high strength in partially recrystallized structures to excellent ductility in fully recrystallized ones, result directly from FHA's ability to manipulate dislocation structures, twin formation, grain boundary density, and precipitate distribution. Thus, FHA induces precise microstructural tuning by balancing recrystallization kinetics, grain refinement, and precipitation effects, ultimately enhancing the synergy between strength and ductility.

A comparison between the product of (UTS x TE, MPa·%) related to YS of the FHAed microstructures for the studied TWIP steel in this research and those of TWIP steels annealed using conventional slow recrystallization treatment, as reported in previous studies [45,53,54], is depicted in Fig. 8. The star data points represent the FAed microstructures in our study. It is evident that the structures attained through FA exhibit notably high UTS × TE values alongside low YS values. An intriguing observation is the increasing trend of UTS × TE values with FHA temperature, specifically T750, T800, and T850. Thus, the values of

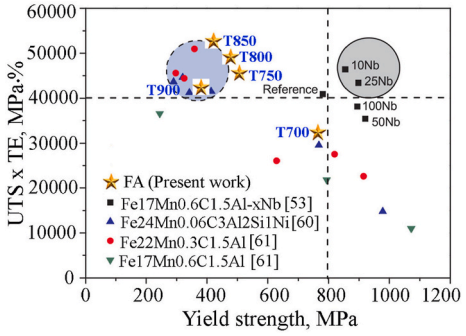

Fig. 8. Illustrates the relationship between UTS × TE and YS in FA structures of the current TWIP steel and partially recrystallized TWIP steels annealed by conventional slow annealing, data quoted from previous studies [45,53,54]. The figure, originally from Ref. [45], has been adopted to include the results of the present study.

UTS × TE demonstrate an increase as YS decreases. This suggests that the combined influence of FHA-treated microstructures and V microalloying can effectively overcome the trade-off between UTS × TE and YS.

3.3. Fracture mechanisms

Fig. 9 presents the fracture surface of the tensile-strained T700 structure. The fracture morphology is characterized by a mixture of a dimple pattern and cleavage features, with large/deep dimples of various shapes, outlined by yellow dotted lines in Fig. 9(a). Notably, a region featuring a flat surface (FS), a sign of quasi-cleavage, is observed in conjunction with these large dimples, as depicted in Fig. 9(a). Upon closer examination in Fig. 9(b) at high magnification, NMIs, indicated by arrows, are visible within several dimples. It is well-established that void nucleation typically occurs when particles detach from the ductile matrix due to incompatibility and peel away during the fracture of the material, ultimately forming a void. The formation of these induced voids is influenced by the size and distribution of NMIs particles. The statistical size and frequency analysis of NMIs are presented in Section 3.4, Inclusion classification and statistical analysis. Furthermore, the volume and shape of dimples change with further straining [55,56]. Even in instances where NMIs do not lead to material failure, they have the potential to introduce voids and stress concentrations, contingent on the relative plasticity [57].

As plastic deformation proceeds, the matrix surrounding these voids remains deformable, allowing the voids to expand into large dimples. Consequently, the fracture surface of the T700 structure is predominantly characterized by the presence of these large dimples, as shown in Fig. 8. Luo and Huang [58] investigated the ductile fracture modes of a coarse-grained structure TWIP steel (Fe-0.6C–22Mn) in comparison with 304 stainless steel (304 ss) and interstitial-free (IF) steel. Their findings indicated that the tensile fracture of the TWIP steel occurs due to plastic instability without the occurrence of necking. This phenomenon is attributed to a few voids nucleating on the NMIs and growing along the tensile direction during uniform plastic deformation. However, the volume fraction of these voids is insufficient to trigger the fracture. Finally, the stress reaches a level high enough to induce plastic instability by forming shear bands.

Similarly, the analysis of the fracture surface for the tensile-strained T850 structure reveals a ductile dimple fracture pattern characterized by numerous large dimples (voids) ranging in size from 5 to 10 μm, as illustrated in Fig. 10(a). A closer examination of the fracture surface in Fig. 10(b) confirms the presence of NMIs within these (black) deep dimples/voids, highlighting their role in the void formation. Notably, the quasi-cleavage shear areas associated with the larger dimples are considerably smaller than those in T700. This reduction is attributed to the softer matrix in T850. A substantial size difference exists between the dimples observed in T700 compared to T850.

SEM analysis of the fracture surfaces revealed predominantly ductile failure features for all FA-treated specimens. The T700 sample, characterized by a high fraction of deformed grains, exhibited large, deep dimples and some quasi-cleavage areas, indicating early plastic instability and limited strain accommodation. The presence of hard regions, i.e., non-recrystallized regions within the matrix, reduces uniform plastic deformation. In contrast, the T850 structure, which exhibits a nearly fully recrystallized fine-grained microstructure, displays a more homogeneous dimpled fracture surface (Fig. 10). The dimples are smaller and more uniformly distributed compared to those in T700, indicating improved ductility and strain accommodation capacity. The recrystallized matrix with a refined grain size (~3 μm) likely enhances strain hardening via the dynamic Hall–Petch effect and delays void coalescence and necking. While NMIs are still present, their influence is less pronounced due to the more compliant and twinned matrix structure, which supports stable plastic flow and resists premature failure.

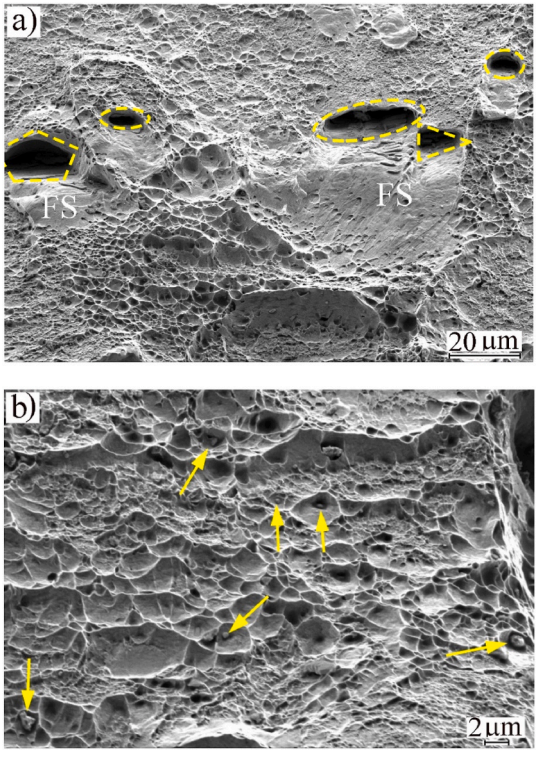

Fig. 9. SEM-images of the fracture surface of the tensile-strained T700 structure: (a) Dimple fracture morphology alongside large/deep dimples of various shapes, highlighted in yellow, (b) a high magnification of the fracture surface showing the presence of NMIs within few dimples. There are dimples where NMIs has left off.

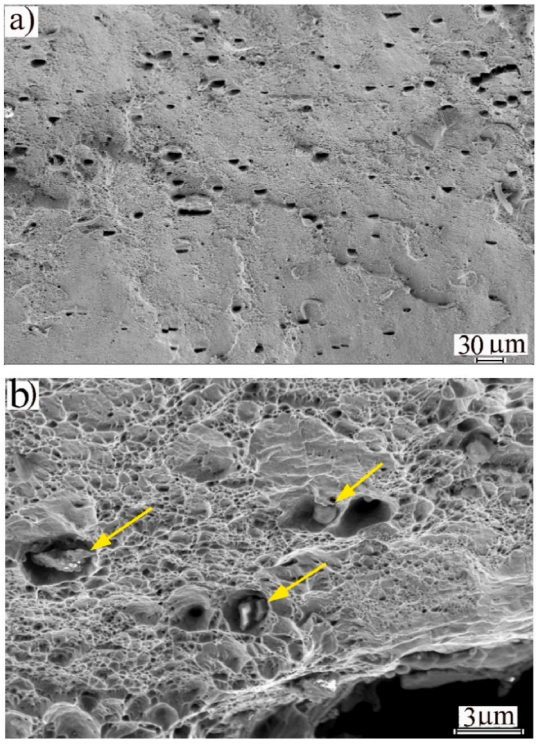

Fig. 10. SEM-images of the fracture surface of the tensile-strained T850 structure: (a) numerous voids of various shapes on ductile dimple fracture surface, (b) high magnification of the fracture surface showing the presence of large NMIs inside some dimples.

The comparison between the two conditions demonstrates a strong dependence of fracture behavior on FHA temperature and resulting microstructure. In particular, the transition from a partially recrystallized to a fully recrystallized structure significantly alters the crack propagation path, shifting from early void growth and quasi-cleavage in T700 to more uniform ductile tearing in T850. This transition is associated with a shift in fracture mode from a mixed (ductile + brittle) failure toward fully ductile failure. These findings further confirm the importance of microstructural control via FHA in tailoring the strength–ductility balance and fracture resistance of high-Mn TWIP steels. The enhanced strain hardening capacity in T850 also helps suppress localized necking and prolong uniform deformation, thereby delaying fracture and promoting energy absorption during tensile loading. These mechanisms emphasize the significant role of microstructure, shaped by FHA conditions, in determining fracture mechanisms and directing crack paths.

As depicted in the tensile flow curves in Fig. 7, the plastic instability of T700 initiates early in the plastic deformation stage, around 0.2 strain, due to its low work-hardening capacity, as shown from the strain-hardening rates illustrated in Fig. 11. Therefore, void nucleation occurs at the initial stages of tensile straining for the T700 structure, which has the lowest fraction, 18 % of partially recrystallized grains, and the highest fraction of hard/deformed grains, 60 %, see Fig. 3.

The evolution of the strain-hardening rate (Fig. 11) reflects the increasing contribution of dislocation–twin interactions with rising FHA temperature. In the T700 structure, the high density of work-hardened dislocations dominates the deformation response, but limited twinning activity results in a relatively short-lived hardening stage. In contrast, specimens annealed at higher temperatures (T850 and T900) exhibit fully recrystallized, fine-grained microstructures that facilitate the early activation of mechanical twinning due to a lower critical resolved shear stress for twinning. These mechanical twins act as dynamic barriers to dislocation motion, segmenting grains and reducing dislocation mean free paths. As deformation proceeds, dislocations accumulate at twin boundaries, promoting strain hardening through kinematic backstress. This twin–dislocation interaction contributes to a sustained hardening rate over a broader strain range, consistent with the observed dynamic Hall–Petch effect. Thus, the more pronounced and prolonged hardening behavior at higher FHA temperatures can be attributed to the combined effects of refined grain size and increased twinning activity.

3.4. Inclusion classification and statistical analysis

Energy-dispersive X-ray spectroscopy (EDS) analysis indicated that the main components of NMIs in the steel included Al_2O_3, MnS, MnSe, TiN, and VN. Each inclusion was categorized based on its molar percentage composition of four key elements: Al_2O_3, Mn(S,Se), TiN, and VN, with a threshold of 5 mol%. To simplify, MnS and MnSe were combined into a single category called Mn(S,Se), while TiN and VN were grouped under (Ti,V)N, recognizing their comparable nitride-forming characteristics and contributions to inclusion creation.

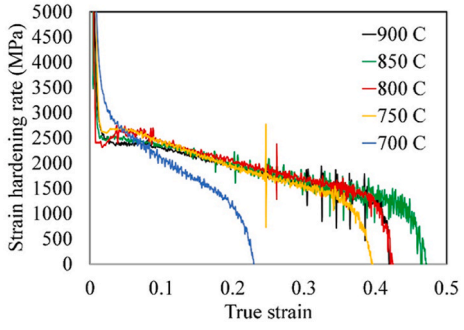

Fig. 11. Strain-hardening rates of the tensile straining structures achieved by FA.

The inclusions displayed irregular, non-spherical shapes, suggesting they formed during solidification and may play a role in heterogeneous nucleation processes. To better understand the behavior of inclusion formation, a classification based on size was utilized: small inclusions (2–5 μm) and large inclusions (>5 μm). The statistical distribution of inclusion types categorized by size is shown in Fig. 12.

Across both size categories, the predominant inclusion type was the mixed Al_2O_3 + Mn(S,Se) phase, making up about 60 % of all inclusions. Mn(S,Se) inclusions ranked as the second most frequent, representing 11 % of small inclusions and 36 % of large ones. These patterns align with findings presented by Liu et al. [59], who identified MnS(Se) and MnS(Se)–Al(O)N aggregates as the primary inclusions (66.7 %) in Fe–25Mn–3Al-2.6Si TWIP steels. Similarly, Aboutalebi et al. [60] reported Mn(S,Se)-based inclusions in CoCrFeMnNi high-entropy alloys. These inclusions featured both single-phase and mixed forms, with Mn–Cr–Al oxide cores, and were present even when high-purity elements were used in the melting process.

Inclusions consisting of (Ti,V)N were particularly noteworthy, especially within the small size range, representing 10 % of all inclusions. This suggests that (Ti,V)N formation is favored during solidification due to Ti and V's strong chemical affinity for nitrogen. Furthermore, complex Mn(S,Se) + (Ti,V)N inclusions accounted for 10 % of the small inclusions and 3 % of the larger ones. Their presence suggests potential post-solidification clustering or co-nucleation behavior.

Ultimately, complex three-phase clusters composed of Al_2O_3, Mn(S, Se), and (Ti,V)N were discovered, particularly in the small inclusion group (8 %) and to a lesser extent in the large group (2 %). This pattern likely suggests a solidification sequence where Al_2O_3 and (Ti,V)N act as heterogeneous nucleation sites for MnS(Se), which typically emerges in the later stages of solidification. The stratified buildup of these complexes emphasizes the importance of chemical composition and cooling pathways in shaping the structure and evolution of inclusions.

3.5. Physically based model

The physical model employed in this work provides a semi-quantitative framework for interpreting the evolution of flow stress based on dislocation mechanisms. While microstructural evolution, mainly varying degrees of recrystallization and twinning, may introduce some uncertainty in parameter accuracy, the model effectively reveals trends in strain hardening and internal stress development. Further refinement of the model would require localized microstructural input and in situ measurements.

The physically based model is evaluated using the experimental stress-strain curves. The flow stresses generated by the model are compared with the experimental true stress-strain curves acquired at various FA temperatures (Fig. 13).

Using this model, we calculated the dislocation density, mean free path, and resulting backstress relative to true strain, which are illustrated in Fig. 14a–c. All specimens began with an initial dislocation density of $1012/m^2$. For samples annealed at 750–900 °C, the density rose to about $10^{15}/m^2$ at a true strain of roughly 0.4, after which it plateaued (see Fig. 14(a)). In contrast, for the specimen annealed at 700 °C, the curve's slope declines at much lower strains, below 0.15, reaching a maximum dislocation density of $6 \times 10^{14}/m^2$ at a true strain of 0.25. According to equation (2), this results in diminished isotropic hardening. Accordingly, as depicted in Fig. 11, this specimen's strain hardening rate (SHR) is lower than that of the other four samples, primarily due to its distinct microstructure. EBSD analysis reveals that only about 20 % of the sample annealed at 700 °C is recrystallized, meaning a substantial portion comprises coarse (non-recrystallized) grains, which correlates with a lower dislocation density and consequently reduced strain hardening.

The dislocation mean free path in each specimen initially equals its

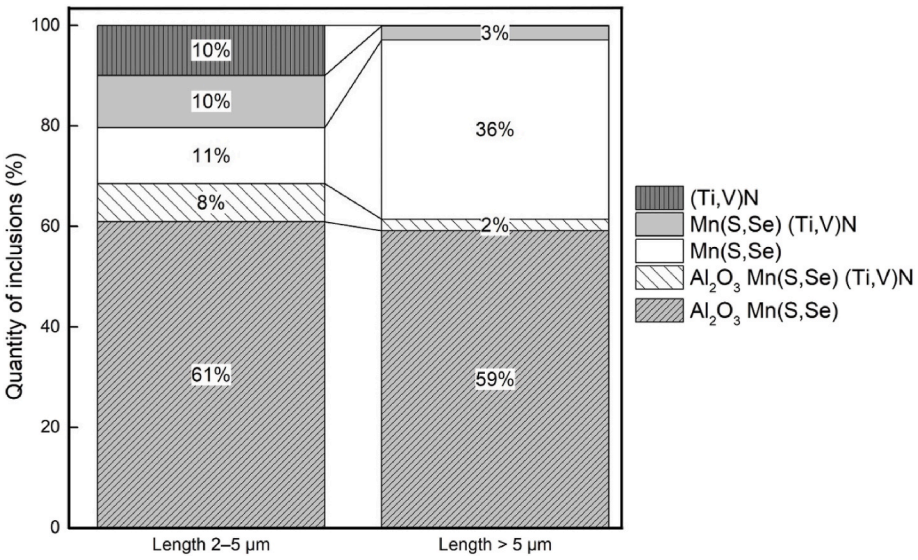

Fig. 12. Distribution of inclusion types in different size categories in the high-Mn TWIP steel.

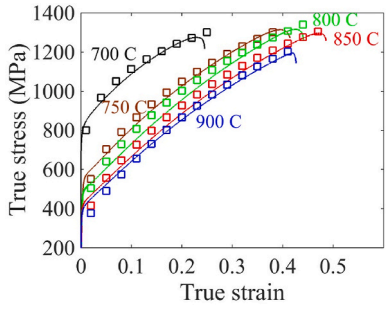

Fig. 13. Comparison between the modeled flow stresses with the experimental data obtained for various annealing temperatures.

grain size (Fig. 14(b)). As deformation progresses, the free path in the specimen annealed at 700 °C is only slightly reduced. However, the dislocation-free path decreases to approximately 20–30 % of the initial value for the other four samples. The mean free path in these specimens experiences a significant reduction at small strains. This is due to the fact that twinning initiation strain (ε_i) is very small in these recrystallized fine-grained specimens. As mentioned in sec. 2.5, small values in the range 0.03–0.04 was considered for ε_i based on ref. [30]. As a result, twinning triggers the dynamic Hall-Petch mechanism at small strains, leading to a reduction of the mean free path. However, the mean free path has soon reached a plateau condition at true strains of ~0.2. This seems reasonable considering the very fine-grained structures obtained here by annealing, as suggested in Ref. [61].

Consistently, SHR values > 2000 MPa is measured up to the same strain (Fig. 11), suggesting that the TWIP mechanism is dominant in this range.

According to equation (3), the reduced mean free path of the dislocations leads to kinematic hardening (backstress), as illustrated in Fig. 14(c). The higher backstress observed in the specimens annealed at 750–900 °C, compared to those treated at 700 °C, can be attributed to their significant reduction in mean free path due to mechanical twinning. A similar outcome was previously reported in the comparison between fine and coarse-grained high-Mn twinning-induced plasticity steels treated by FA [23]. According to Fig. 14 (c), for the specimens annealed at 850 and 900 °C, kinematic hardening has reached approximately 30 % of the total flow stress. Experimental evidence for this contribution from the backstress in high-Mn TWIP steel has been previously provided by Ref. [30].

The increased backstress observed in specimens annealed at 750–900 °C is attributed to strain partitioning between recrystallized and deformed grains in partially recrystallized structures (750–800 °C), as well as enhanced mechanical twinning in fine-grained, fully recrystallized structures (850–900 °C). Both mechanisms promote the accumulation of geometrically necessary dislocations and internal stresses, manifesting as kinematic hardening. In contrast, the 700 °C sample, characterized by a predominantly deformed structure and limited twinning, exhibits lower strain incompatibility and, consequently, lower backstress.

The dynamic Hall–Petch effect is essential for enhancing strain hardening in FA-treated TWIP steels by refining the mean free path of dislocations via mechanical twinning. Mechanical twins quickly form during plastic deformation in fine-grained, fully recrystallized austenitic structures, especially those produced at elevated FHA temperatures (e.g., 850–900 °C). These twins act as effective barriers to dislocation movement, akin to grain boundaries, which subdivide grains into smaller subdomains and significantly decrease the mean free path of dislocations. The microstructural refinement caused by twins results in an increase in dislocation density, which, in turn, improves kinematic hardening (backstress). Our strain-hardening rate curves and modeling results indicate that this effect sustains high work-hardening rates across a broad strain range, delaying necking and enhancing the overall synergy of strength and ductility balance. The early onset of twinning in fine grains, coupled with restricted grain growth during the brief FA duration, emphasizes the vital role of twinning in both activating and sustaining the dynamic Hall–Petch effect during tensile deformation.

The Hall-Petch equation ($\sigma = \sigma_0 + K_{H-P} \cdot d^{-1/2}$) was fitted to the flow stress-strain data of each sample to calculate the Hall-Petch constant (K_{H-P}) versus true strain, as presented in Fig. 14(d). The values of dislocations mean free path (Fig. 14(b)) were used as the instantaneous grain size (d), and the initial YS values, as mentioned in Table 2, were implemented for σ_0. The slope of H–P relationship is initially high and diminishes with the progress of deformation for all specimens. This is due to the saturation of the twinned microstructure at high strains, as also predicted by the mean free path of dislocations (Fig. 14(b)).

In TWIP steels, the enhanced strain hardening behavior is significantly influenced by the interplay between dislocation movement and deformation twinning. According to De Cooman et al. [62], dislocation glide remains the primary mechanism of plastic deformation, while the formation of deformation twins notably alters dislocation dynamics by reducing the effective mean free path of dislocations. This results in the

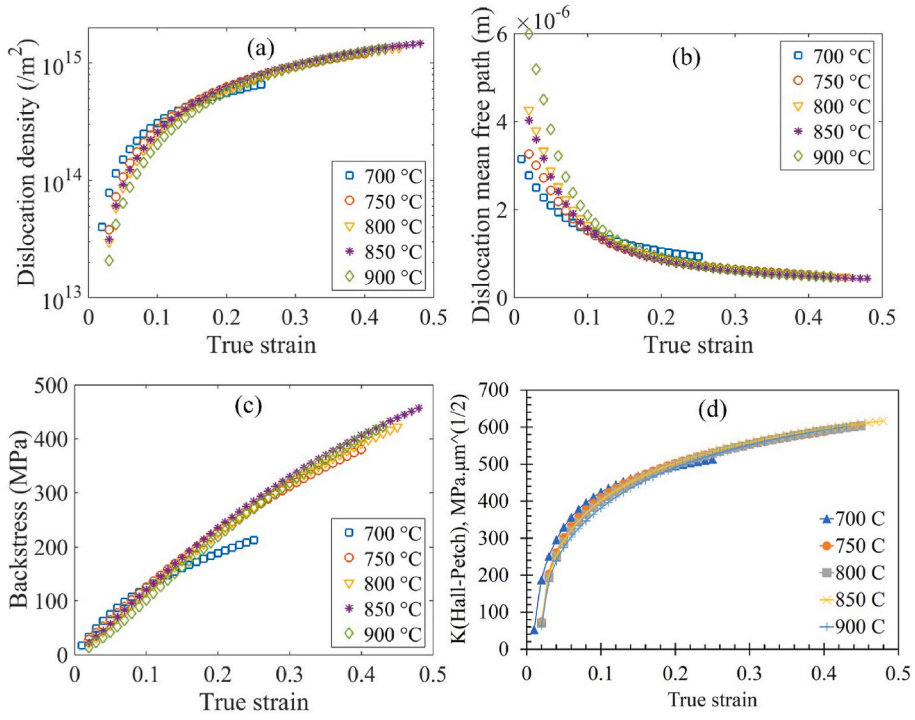

Fig. 14. The variations of a) dislocation density, b) dislocation mean free path, (c) kinematic hardening (backstress) with true strain as predicted by the model, and (d) the strengthening effect of reduced dislocation free path in terms of the Hall-Petch constant.

"dynamic Hall–Petch effect," where the continuous formation of twins simulates grain refinement, thereby increasing flow stress and strain hardening. Additionally, twin boundaries are formidable obstacles to dislocation movement, prompting dislocation pile-ups and substantial internal back stresses. This process, coupled with the formation of dense twin structures that interact with the existing dislocation substructure, promotes ongoing strain hardening during plastic deformation. The interaction of reduced mean free path, kinematic hardening, and stress distribution between twin and matrix regions underscores the vital role of twin–dislocation interactions in maintaining the strength–ductility synergy characteristic of TWIP steels. According to Bouaziz et al. [63], understanding the unique work-hardening characteristics of TWIP (Twinning-Induced Plasticity) steels hinges on the dynamic Hall–Petch effect and dislocation–twin interactions. The authors indicate that mechanical twins serve as dynamic obstacles to dislocation movement, thus refining the microstructure during plastic deformation. This interaction reduces the mean free path of dislocations, thereby enhancing strain hardening in a manner akin to how grain refinement strengthens materials within the context of the classical Hall–Petch relationship. The interplay between dislocation–twin interactions and the evolving microstructure is crucial to the distinctive mechanical response of TWIP steels, confirming the dynamic Hall–Petch effect as a solid framework for elucidating their behavior.

4. Conclusions

This study investigates the effects of fast heating annealing (FHA) on the microstructural evolution and mechanical properties of V-microalloyed high-Mn TWIP steel. Applying FH (200 °C/s) and short annealing durations (30 s) across a temperature range of 700 °C–900 °C revealed significant enhancements in microstructure and mechanical performance. The following findings underscore the potential of FHA as an effective processing technique to optimize the properties of TWIP steels for advanced structural and industrial applications.

1. Partial recrystallization is observed at 700°C-800 °C, while fully recrystallized fine-grained structures are achieved at higher temperatures (850°C-900 °C), resulting in grain refinement and enhanced mechanical properties.
2. Optimal mechanical properties were achieved at FHA 850 °C, displaying high elongation (60 %), yield strength (415 MPa), and tensile strength (850 MPa). This combination demonstrated the highest product of strength and ductility (TS × TE = 50,700 MPa·%) compared to other conditions and literature data.
3. Although this study did not directly compare fast and slow heating, it emphasizes significant microstructural and mechanical responses associated with FHA, referencing existing literature on conventional annealing. The findings indicate that FHA promotes the formation of ultrafine grain structures and optimized recrystallization states, leading to a better balance of strength and ductility in TWIP steel.
4. The physically based model of the tensile flow curves indicates that the activation of the mechanical twinning mechanism during deformation induces a dynamic Hall-Petch effect, which shortens dislocation mean free paths. This process substantially increases strain hardening rates, thereby enhancing the strength of the steel.
5. Fracture surface analysis reveals a predominantly ductile fracture mechanism, characterized by dimples with NMIs as void nucleation sites. The enhanced mechanical properties reduce the detrimental effects of NMIs by promoting mechanical twinning, delaying necking and failure.

Declaration of competing interest

The authors declare that they have no known competing financial interests or personal relationships that could have appeared to influence the work reported in this paper.

Acknowledgments

The authors gratefully acknowledge the Materials and Mechanical Engineering (MME) at the University of Oulu for providing technical

support in conducting the rolling processes and thermal cycles using the Gleeble simulator.

References

[1] Zhao J, Jiang Z. Thermomechanical processing of advanced high strength steels. Prog Mater Sci 2018;94:174–242. https://doi.org/10.1016/j.pmatsci.2018.01.006.

[2] De Cooman BC, Chin K, Kim J. High Mn TWIP steels for automotive applications. New Trends Dev. Automot. Syst. Eng 2011. https://doi.org/10.5772/14086.

[3] Güvenç O, Roters F, Hickel T, Bambach M. ICME for crashworthiness of TWIP steels: from Ab Initio to the crash performance. JOM 2015;67:120–8. https://doi.org/10.1007/S11837-014-1192-8.

[4] Wesselmecking S, Kreins M, Dahmen M, Bleck W. Material oriented crash-box design – combining structural and material design to improve specific energy absorption. Mater Des 2022;213:110357. https://doi.org/10.1016/J.MATDES.2021.110357.

[5] De Cooman BC, Estrin Y, Kim SK. Twinning-induced plasticity (TWIP) steels. Acta Mater 2018;142:283–362. https://doi.org/10.1016/j.actamat.2017.06.046.

[6] Shao CW, Zhang P, Zhu YK, Zhang ZJ, Pang JC, Zhang ZF. Improvement of low-cycle fatigue resistance in TWIP steel by regulating the grain size and distribution. Acta Mater 2017;134:128–42. https://doi.org/10.1016/J.ACTAMAT.2017.05.004.

[7] Guo X, Mao N, Kong T, Zhang J, Shen J, Wang C, Sun C, Li P, Xiong Z. Strain rate-dependent plastic behavior of TWIP steel investigated by crystal plasticity model. Mater. Sci. Eng. A. 2023:145986. https://doi.org/10.1016/J.MSEA.2023.145986.

[8] Feng X, Liu X, Bai S, Tang Y, Ye Y. Investigation of dynamic tensile mechanical responses and deformation mechanism at high strain rates in a TWIP steel. J Mater Res Technol 2023;26:639–53. https://doi.org/10.1016/J.JMRT.2023.07.241.

[9] Feng X, Liu X, Bai S, Ye Y, Zong L, Tang Y. Mechanical properties and deformation behaviour of TWIP steel at different strain rates. Mater. Sci. Eng. A. 2023;879:145182. https://doi.org/10.1016/j.msea.2023.145182.

[10] Hamada AS, Kisko A, Khosravifard A, Hassan MA, Karjalainen LP, Porter D. Ductility and formability of three high-Mn TWIP steels in quasi-static and high-speed tensile and Erichsen tests. Mater. Sci. Eng. A. 2018;712:255–65. https://doi.org/10.1016/J.MSEA.2017.11.111.

[11] Sklate Boja MF, Giordana MF, Malarria J, Druker AV. Procedures for microstructurally conditioning an Fe-22Mn-0.6C-1.5Al TWIP steel for optimal mechanical behaviour, Mater. Charact 2023;199:112790. https://doi.org/10.1016/j.matchar.2023.112790.

[12] Mattos Ferreira V, Mecozzi MG, Petrov RH, Sietsma J. Microstructure development of pearlitic railway steels subjected to fast heating. Mater Des 2022;221:110989. https://doi.org/10.1016/j.matdes.2022.110989.

[13] Vercruysse F, Castro Cerda FM, Verleysen P, Petrov RH. Behavior of ultrafast annealed advanced high strength steels under static and dynamic conditions. Mater. Sci. Eng. A. 2020;780:139168. https://doi.org/10.1016/J.MSEA.2020.139168.

[14] Thomas LS, Matlock DK. Formation of banded microstructures with rapid intercritical annealing of cold-rolled sheet steel. Metall. Mater. Trans. A Phys. Metall. Mater. Sci. 2018;49:4456–73. https://doi.org/10.1007/s11661-018-4742-9.

[15] Dai J, Meng Q, Zheng H. High-strength dual-phase steel produced through fast-heating annealing method. Results Mater 2020;5:100069. https://doi.org/10.1016/j.rinma.2020.100069.

[16] Kulakov M, Poole WJ, Militzer M. The effect of the initial microstructure on recrystallization and austenite formation in a DP600 steel. Metall. Mater. Trans. A Phys. Metall. Mater. Sci. 2013;44:3564–76. https://doi.org/10.1007/S11661-013-1721-Z/TABLES/6.

[17] Papaefthymiou S, Banis A, Bouzouni M, Petrov RH. Effect of ultra-fast heat treatment on the subsequent formation of mixed martensitic/bainitic microstructure with carbides in a CrMo medium carbon steel. Met. 2019;9:312. https://doi.org/10.3390/MET9030312. 9 (2019) 312.

[18] Yuan Q, Ren J, Mo J, Zhang Z, Tang E, Xu G, Xue Z. Effects of rapid heating on the phase transformation and grain refinement of a low-carbon mciroalloyed steel. J Mater Res Technol 2023;23:3756–71. https://doi.org/10.1016/J.JMRT.2023.02.018.

[19] Wang J, El-Fallah GMAM, Wang Z, Li H, Dong H, Tao Q. Strength improvement over 2 GPa and austenite grain ultra-refinement in a low carbon martensite steel achieved by ultra-rapid heating and quenching. Mater. Sci. Eng. A. 2023;884:145538. https://doi.org/10.1016/j.msea.2023.145538.

[20] Meng Q, Li J, Zheng H. High-efficiency fast-heating annealing of a cold-rolled dual-phase steel. Mater Des 2014;58:194–7. https://doi.org/10.1016/j.matdes.2014.01.055.

[21] Dai J, Meng Q, Zheng H. An innovative pathway to produce high-performance quenching and partitioning steel through ultra-fast full austenitization annealing. Mater Today Commun 2020;25:101272. https://doi.org/10.1016/J.MTCOMM.2020.101272.

[22] Matlock DK, Kang S, De Moor E, Speer JG. Applications of rapid thermal processing to advanced high strength sheet steel developments. Mater Char 2020;166:110397. https://doi.org/10.1016/j.matchar.2020.110397.

[23] Khosravifard A, Hamada A, Järvenpää A, Karjalainen P. Enhancement of grain structure and mechanical properties of a high-Mn twinning-induced plasticity steel bearing Al–Si by fast-heating annealing. Mater. Sci. Eng. A. 2020;795:139949. https://doi.org/10.1016/J.MSEA.2020.139949.

[24] Järvenpää A, Ghosh S, Khosravifard A, Jaskari M, Hamada A. A new processing route to develop nano-grained structure of a TRIP-aided austenitic stainless-steel using double reversion fast-heating annealing. Mater. Sci. Eng. A. 2021;808:140917. https://doi.org/10.1016/j.msea.2021.140917.

[25] Hamada A, Khosravifard A, Ghosh S, Jaskari M, Järvenpää A, Karjalainen P. High-Speed Erichsen testing of grain-refined 301LN austenitic stainless steel processed by double-reversion annealing. Metall. Mater. Trans. A Phys. Metall. Mater. Sci. 2022;53:2174–94. https://doi.org/10.1007/s11661-022-06659-5.

[26] Hamada AS, Jaskari M, Ali M, Kaijalainen A, Järvenpää A. Impact of ultra-flash tempering treatment on the microstructure and mechanical properties of high-strength carbon steel. Mater Sci Forum 2023;1105:53–9. https://doi.org/10.4028/P-SP4FFB.

[27] Liu G, Li T, Yang Z, Zhang C, Li J, Chen H. On the role of chemical heterogeneity in phase transformations and mechanical behavior of flash annealed quenching & partitioning steels. Acta Mater 2020;201:266–77. https://doi.org/10.1016/j.actamat.2020.10.007.

[28] Sun WW, Wu YX, Yang SC, Hutchinson CR. Advanced high strength steel (AHSS) development through chemical patterning of austenite. Scr Mater 2018;146:60–3. https://doi.org/10.1016/J.SCRIPTAMAT.2017.11.007.

[29] Belde M, Springer H, Raabe D. Vessel microstructure design: a new approach for site-specific core-shell micromechanical tailoring of TRIP-assisted ultra-high strength steels. Acta Mater 2016;113:19–31. https://doi.org/10.1016/J.ACTAMAT.2016.04.051.

[30] Bouaziz O, Allain S, Scott C. Effect of grain and twin boundaries on the hardening mechanisms of twinning-induced plasticity steels. Scr Mater 2008;58:484–7. https://doi.org/10.1016/J.SCRIPTAMAT.2007.10.050.

[31] Zhao GH, Xu X, Dye D, Rivera-Díaz-del-Castillo PEJ. Microstructural evolution and strain-hardening in TWIP Ti alloys. Acta Mater 2020;183:155–64. https://doi.org/10.1016/J.ACTAMAT.2019.11.009.

[32] Steinmetz DR, Jäpel T, Wietbrock B, Eisenlohr P, Gutierrez-Urrutia I, Saeed-Akbari A, Hickel T, Roters F, Raabe D. Revealing the strain-hardening behavior of twinning-induced plasticity steels: theory, simulations, experiments. Acta Mater 2013;61:494–510. https://doi.org/10.1016/J.ACTAMAT.2012.09.064.

[33] Sahu P, Hamada AS, Sahu T, Puustinen J, Oittinen T, Karjalainen LP. Martensitic transformation during cold rolling deformation of an austenitic Fe-26Mn-0.14C alloy. Metall. Mater. Trans. A Phys. Metall. Mater. Sci. 2012;43:47–55. https://doi.org/10.1007/s11661-011-0818-5.

[34] Bracke L, Verbeken K, Kestens L, Penning J. Microstructure and texture evolution during cold rolling and annealing of a high Mn TWIP steel. Acta Mater 2009;57:1512–24. https://doi.org/10.1016/j.actamat.2008.11.036.

[35] Liu JB, Liu XH, Liu W, Zeng YW, Shu KY. Microstructure and hardness evolution during isothermal process at 700 °C for Fe–24Mn–0.7Si–1.0Al TWIP steel. Mater Char 2010;61:1356–8. https://doi.org/10.1016/J.MATCHAR.2010.09.007.

[36] Behjati P, Kermanpur A, Karjalainen LP, Järvenpää A, Jaskari M, Samaei Baghbadorani H, Najafizadeh A, Hamada A. Influence of prior cold rolling reduction on microstructure and mechanical properties of a reversion annealed high-Mn austenitic steel. Mater. Sci. Eng. A. 2016;650:119–28. https://doi.org/10.1016/J.MSEA.2015.09.069.

[37] Hamada A, Juuti T, Khosravifard A, Kisko A, Karjalainen P, Porter D, Kömi J. Effect of silicon on the hot deformation behavior of microalloyed TWIP-type stainless steels. Mater Des 2018;154:117–29. https://doi.org/10.1016/J.MATDES.2018.05.029.

[38] Yanushkevich Z, Belyakov A, Kaibyshev R, Haase C, Molodov DA. Effect of cold rolling on recrystallization and tensile behavior of a high-Mn steel. Mater Char 2016;112:180–7. https://doi.org/10.1016/J.MATCHAR.2015.12.021.

[39] Scott C, Remy B, Collet JL, Cael A, Bao C, Danoixd F, Malardc B, Curfse C. Precipitation strengthening in high manganese austenitic TWIP steels. Int J Mater Res 2011;102:538–49. https://doi.org/10.3139/146.110508/MACHINEREADABLECITATION/RIS.

[40] Zhang G, Wang S, Li B, Chen B, Zhang B, Zhang X, Ma M, Liu R. Achieving high strength and ductility in Fe–Mn–Al–C austenitic steel via vanadium microalloying and aging. J Mater Res Technol 2023;24:8443–57. https://doi.org/10.1016/J.JMRT.2023.05.090.

[41] Yue H, Peng Z, Wang H, Zhao Z, Lu H, Tang Y, An F, Zhang J, Zhang X, Liu R. Effect of carbide precipitation on the twin behavior and work hardening capability of Fe-20Mn-2Al-0.4C-0.7V steel. Vacuum 2025;239:114346. https://doi.org/10.1016/J.VACUUM.2025.114346.

[42] Allam T, Guo X, Lipinska-Chwalek M, Hamada A, Ahmed E, Bleck W. Impact of precipitates on the hydrogen embrittlement behavior of a V-alloyed medium-manganese austenitic stainless steel. J Mater Res Technol 2020;9:13524–38. https://doi.org/10.1016/J.JMRT.2020.09.085.

[43] Jo MC, Jo MC, Zargaran A, Sohn SS, Kim NJ, Lee S. Effects of Al addition on tensile properties of partially recrystallized austenitic TRIP/TWIP steels. Mater. Sci. Eng. A. 2021;806:140823. https://doi.org/10.1016/j.msea.2021.140823.

[44] Lan P, Zhang J. Tensile property and microstructure of Fe-22Mn-0.5C TWIP steel. Mater. Sci. Eng. A. 2017;707:373–82. https://doi.org/10.1016/J.MSEA.2017.09.061.

[45] Gwon H, Kim JK, Jian B, Mohrbacher H, Song T, Kim SK, De Cooman BC. Partially-recrystallized, Nb-alloyed TWIP steels with a superior strength-ductility balance. Mater. Sci. Eng. A. 2018;711:130–9. https://doi.org/10.1016/J.MSEA.2017.11.012.

[46] Kang S, Jung YS, Jun JH, Lee YK. Effects of recrystallization annealing temperature on carbide precipitation, microstructure, and mechanical properties in Fe–18Mn–0.6C–1.5Al TWIP steel. Mater. Sci. Eng. A. 2010;527:745–51. https://doi.org/10.1016/J.MSEA.2009.08.048.

[47] Santos DB, Gonzalez BM, Pereloma EV. Recrystallization and mechanical behavior of high Mn and low C cold rolled and annealed steel with TWIP effect. Mater Sci

Forum 2012;715–716:579–84. https://dx.doi.org/10.4028/www.scientific.net/MSF.715-716.579.
[48] Gwon H, Kim JK, Shin S, Cho L, De Cooman BC. The effect of vanadium micro-alloying on the microstructure and the tensile behavior of TWIP steel. Mater. Sci. Eng. A. 2017;696:416–28. https://doi.org/10.1016/J.MSEA.2017.04.083.
[49] Zhong L, Wang Z, Luo Q, Liu W. Effects of cerium addition on the microstructure, mechanical properties and strain hardening behavior of TWIP steel Fe-18Mn-0.6C. Mater Char 2022;183:111626. https://doi.org/10.1016/J.MATCHAR.2021.111626.
[50] Kim JG, Hong S, Anjabin N, Park BH, Kim SK, Chin KG, Lee S, Kim HS. Dynamic strain aging of twinning-induced plasticity (TWIP) steel in tensile testing and deep drawing. Mater. Sci. Eng. A. 2015;633:136–43. https://doi.org/10.1016/J.MSEA.2015.03.008.
[51] Lan P, Zhang J. Twinning and dynamic strain aging behavior during tensile deformation of Fe-Mn-C TWIP steel. Mater. Sci. Eng. A. 2017;700:250–8. https://doi.org/10.1016/J.MSEA.2017.06.012.
[52] Grässel O, Krüger L, Frommeyer G, Meyer LW. High strength Fe-Mn-(Al, Si) TRIP/TWIP steels development - properties - application. Int J Plast 2000;16:1391–409. https://doi.org/10.1016/S0749-6419(00)00015-2.
[53] Santos DB, Saleh AA, Gazder AA, Carman A, Duarte DM, Ribeiro ÉAS, Gonzalez BM, Pereloma EV. Effect of annealing on the microstructure and mechanical properties of cold rolled Fe–24Mn–3Al–2Si–1Ni–0.06C TWIP steel. Mater. Sci. Eng. A. 2011;528:3545–55. https://doi.org/10.1016/J.MSEA.2011.01.052.
[54] Haase C, Ingendahl T, Güvenç O, Bambach M, Bleck W, Molodov DA, Barrales-Mora LA. On the applicability of recovery-annealed Twinning-Induced Plasticity steels: potential and limitations. Mater. Sci. Eng. A. 2016;649:74–84. https://doi.org/10.1016/J.MSEA.2015.09.096.
[55] De Cooman BC, Estrin Y, Kim SK. Twinning-induced plasticity (TWIP) steels. Acta Mater 2018;142:283–362. https://doi.org/10.1016/J.ACTAMAT.2017.06.046.
[56] Lorthios J, Mazière M, Lemoine X, Cugy P, Besson J, Gourgues-Lorenzon AF. Fracture behaviour of a Fe–22Mn–0.6C–0.2V austenitic TWIP steel. Int J Mech Sci 2015;101–102:99–113. https://doi.org/10.1016/J.IJMECSCI.2015.07.029.
[57] Madivala M, Schwedt A, Wong SL, Roters F, Prahl U, Bleck W. Temperature dependent strain hardening and fracture behavior of TWIP steel. Int J Plast 2018;104:80–103. https://doi.org/10.1016/J.IJPLAS.2018.02.001.
[58] Luo ZC, Huang MX. Revealing the fracture mechanism of twinning-induced plasticity steels. Steel Res Int 2018;89:1–7. https://doi.org/10.1002/srin.201700433.
[59] Liu H, Liu J, Michelic SK, Shen S, Su X, Wu B, Ding H. Characterization and analysis of non-metallic inclusions in low-carbon Fe–Mn–Si–Al TWIP steels. Steel Res Int 2016;87:1723–32. https://doi.org/10.1002/srin.201600131.
[60] Aboutalebi MR, Isac M, Guthrie RIL. The behaviour of selenium impurities during the addition of se-containing manganese to steel melt. Steel Res Int 2004;75:366–72. https://doi.org/10.1002/srin.200405782.
[61] Chen J, Dong FT, Liu ZY, Wang GD. Grain size dependence of twinning behaviors and resultant cryogenic impact toughness in high manganese austenitic steel. J Mater Res Technol 2021;10:175–87. https://doi.org/10.1016/J.JMRT.2020.12.030.
[62] De Cooman BC, Estrin Y, Kim SK. Twinning-induced plasticity (TWIP) steels. Acta Mater 2018;142:283–362. https://doi.org/10.1016/J.ACTAMAT.2017.06.046.
[63] Bouaziz O, Allain S, Scott CP, Cugy P, Barbier D. High manganese austenitic twinning induced plasticity steels: a review of the microstructure properties relationships. Curr Opin Solid State Mater Sci 2011;15:141–68. https://doi.org/10.1016/J.COSSMS.2011.04.002.